

Effects of lateral diffusion on morphology and dynamics of a microscopic lattice-gas model of pulsed electrodeposition

Stefan Frank, Daniel E. Roberts, and Per Arne Rikvold

Center for Materials Research and Technology

School of Computational Science and

Department of Physics, Florida State University, Tallahassee, FL 32306-4350, USA

(Dated: July 2, 2018)

The influence of nearest-neighbor diffusion on the decay of a metastable low-coverage phase (monolayer adsorption) in a square lattice-gas model of electrochemical metal deposition is investigated by kinetic Monte Carlo simulations. The phase-transformation dynamics are compared to the well-established Kolmogorov–Johnson–Mehl–Avrami theory [A. N. Kolmogorov, *Bull. Acad. Sci. USSR, Phys. Ser.* **1**, 335 (1937); W. A. Johnson and R. F. Mehl, *Trans. Am. Inst. Min. Metall. Eng.* **135**, 416 (1939); M. Avrami, *J. Chem. Phys.* **7**, 1103 (1939); **8**, 212 (1940); **9**, 177 (1941)]. The phase transformation is accelerated by diffusion, but remains in accord with the theory for continuous nucleation up to moderate diffusion rates. At very high diffusion rates the phase-transformation kinetic shows a crossover to instantaneous nucleation. Then, the probability of medium-sized clusters is reduced in favor of large clusters. Upon reversal of the supersaturation, the adsorbate desorbs, but large clusters still tend to grow during the initial stages of desorption. Calculation of the free energy of subcritical clusters by enumeration of lattice animals yields a quasi-equilibrium distribution which is in reasonable agreement with the simulation results. This is an improvement relative to classical droplet theory, which fails to describe the distributions, since the macroscopic surface tension is a bad approximation for small clusters.

PACS numbers: 68.43.Jk 68.43.Mn 81.15.Pq 82.60.Nh

I. INTRODUCTION

Kinetic lattice-gas models are a valuable tool for the modeling of nucleation and growth of adsorbate layers.^{1,2,3} In electrochemical systems, due to the presence of solvents and counter ions, common models are often more severe simplifications compared to surface science in ultra-high vacuum. It is also more difficult to estimate model parameters from first principles.^{4,5} Though such estimations might seem desirable, they are not mandatory, and simpler ones, for example by fits to experiments, may be used, at least as a start.^{6,7} In spite of these complications, successful applications of the method to electrochemical systems are encouraging (see, e.g., Refs. 6,8). In addition, taking a more fundamental point of view, such truly microscopic models – and the equivalent two-dimensional Ising models – may be compared to prevalent theories of nucleation and growth like the Kolmogorov–Johnson–Mehl–Avrami (KJMA) theory of phase transformations,^{9,10,11,12,13} thus enabling one to investigate the latter’s validity and underlying assumptions.^{14,15,16} The validity of the KJMA theory has been established not too far below the critical temperature over a wide range of magnetic fields (corresponding to supersaturation in the lattice-gas language).^{14,15,16} However, only spin-flip (adsorption/desorption) moves have been included in the dynamics. In the present work, we extend these numerical studies to the effects of lateral adsorbate diffusion to nearest-neighbor positions (corresponding to spin-exchange moves in magnetic language).

Our work is also inspired by recent electrochemical pulse experiments on the dynamics of the processes that occur after lifting the $(22 \times \sqrt{3})$ reconstruction of the Au(111) surface.¹⁷ In that study, during a short positive pulse of the electrode potential, the reconstruction is lifted immediately, and excess Au atoms are released onto the then (1×1) substrate, where they quickly nucleate and form islands. After the pulse, the surface slowly reconstructs again, consuming the excess ions. During this process, however, the adsorbate structure still undergoes post-deposition dynamics, where small islands tend to decay faster, and large islands gain in size before they eventually decay. However, we emphasize that the connection of our model to these experiments is only qualitative. As the source for the adsorbate, we use ions from the solution, whose supersaturation can be pulsed. Moreover, we neglect the geometry of the surface and the dynamics of the lifting and reconstruction process. Also, the peak coverages in our simulations are much higher than in the experiment. We rather focus on the general characteristics of the growth and subsequent decay of submonolayer adsorbates with attractive interactions during and after a pulse of their supersaturation, and how these characteristics compare to the KJMA theory. Though we keep the model as simple as possible, nearest-neighbor diffusion is an essential characteristic of the experimental system and must be included in the dynamics of the model.

We shall not repeat here the discussion of the theory of the decay of metastable phases (see, e.g., Refs. 15,18), but only give a brief summary. The KJMA theory in its simplest form describes the decay of a metastable phase to an

equilibrium phase, driven by a difference in free energy, from simple basic assumptions: negligibly small nuclei form at random and subsequently grow isotropically to larger droplets. An extended volume is defined as the sum of the volumes of all droplets, which grow and overlap freely, even upon collision. Since the nucleation events are completely random, they can also occur in the already transformed volume. The true transformed volume is the space covered by at least one droplet. Due to the randomness of the process, the relation between the extended volume fraction φ_{ext} and the (true) transformed volume fraction φ can be shown to be¹²

$$1 - \varphi = \exp(-\varphi_{\text{ext}}). \quad (1)$$

Assuming a constant radial growth velocity v and a constant nucleation rate I (corresponding to continuous nucleation), the extended volume is, in two dimensions,

$$\varphi_{\text{ext}} = \frac{\pi I v^2 t^3}{3}, \quad (2)$$

at time t after the beginning of the phase transformation. Continuous nucleation is often associated with homogeneous nucleation due to thermal fluctuations. Another case, initial nucleation, where all the nuclei are present at the very beginning of the transformation, is often associated with heterogeneous nucleation at defects. In the case of continuous nucleation, thermal fluctuations that lead to the formation of small droplets obey metastable thermodynamics, and knowledge of the size dependence of the free energy F of compact small droplets is needed. In a mesoscopic description, which should hold sufficiently below the critical temperature, this is obtained as a sum of a surface and a volume term. In two dimensions, this becomes

$$F(r) = 2\pi r \sigma_0 - (\mu - \mu_0) \Delta\theta \pi r^2, \quad (3)$$

for a cluster with effective radius r and surface tension σ_0 along a primitive lattice vector at equilibrium (whose zero-field Ising analog is known exactly¹⁹). The difference in coverage $\Delta\theta$ between the two degenerate equilibrium phases corresponds to the difference of the spontaneous magnetization of the two degenerate phases at zero field in the Ising model.²⁰ The use of the zero-field values is believed to be justified, and a recent publication²¹ supports the point of view that the surface tension is not strongly field dependent (though that study addresses a lower temperature). Conversely, the use of the macroscopic surface tension for microscopic structures is questionable, and more accurate expressions are a matter of research^{22,23,24,25} and are sought in this paper as well. The free energy has a maximum at the critical droplet size (volume) s^* . The existence of this maximum is the reason why the phase transformation is activated. On average, when smaller than s^* , the droplets tend to dissolve, and when greater than s^* , they tend to grow. The critical droplet size is a statistical quantity and is less sharply defined the flatter the shape of the maximum of the free energy.

The velocity and the ratio of nucleation and growth are influenced by lateral mass transport. In ultra-high vacuum (UHV) and under the impact of a constant flux of the adsorbate, desorption may often be neglected (irreversible growth). In electrochemistry (EC), where the control parameter is the electrochemical potential, quasi-equilibrium is established for the subcritical fluctuations, so that desorption has to be included in a model description (reversible growth). As a consequence, in UHV, surface diffusion is generally the only means of lateral mass transport, while in EC, it can as well occur through the solution by independent desorption and adsorption events at different locations. In surface science, it has long been established that diffusion introduces correlations between clusters, since it reduces the nucleation probability in the vicinity of existing islands.^{3,26} Recent publications have addressed this violation of the basic assumptions of KJMA kinetics.^{27,28} Since the number of nucleation events is effectively *diminished*, phase transformation is slowed down. However, it has not been considered that the enhanced mass transport can *increase* the nucleation and growth rates, resulting in an acceleration of phase transformation. Thus, truly microscopic model calculations are desirable, and we provide them in this paper. This microscopic approach distinguishes our work from most other studies that aim at generalizing the KJMA theory.

The rest of this paper is organized as follows: We introduce the model and describe our model calculations in Sec. II. Results are presented in Sec. III. First, we discuss the phase-transformation kinetics (Sec. III A) and how they are affected by diffusion. Second, we discuss the effects of diffusion on the size distributions of supercritical (Sec. III B) and subcritical (Sec. III C) clusters. For the latter, we give a theoretical explanation in terms of the free energy of lattice animals. A summary and conclusions follow in Sec. IV.

II. MODEL AND ALGORITHM

A. Model

We describe the electrochemical deposition of ions onto a metal surface in terms of a square lattice-gas model with attractive nearest-neighbor interactions. The grand-canonical Hamiltonian of the system reads

$$\mathcal{H} = -\phi \sum_{\langle i,j \rangle} c_i(t)c_j(t) - \mu \sum_i c_i(t), \quad (4)$$

where ϕ is the interaction constant and μ the adsorbing ions' electrochemical potential in the solution, which represents an infinite reservoir. The c_i are occupation variables at site i with the values

$$c_i(t) = \begin{cases} 0 & \text{if empty} \\ 1 & \text{if occupied.} \end{cases}$$

The first sum in Eq. (4) runs over all pairs of nearest-neighbor sites, and the second runs over all lattice sites. Water and counter ions are not explicitly included. The Hamiltonian is equivalent to the Ising model, up to an additive factor.^{18,29,30}

We perform model simulations for an $L \times L = 256 \times 256$ square lattice, applying periodic boundary conditions, for the values of the model parameters $\phi = 4$, and $|\mu - \mu_0| = 0.4$,³¹ where μ_0 is the electrochemical potential at coexistence, and $\mu > \mu_0$ favors adsorption. The temperature T equals $0.8 T_c \approx 0.453873 \phi \approx 1.815348 J$,³⁰ with T_c the critical temperature of the Ising model for the given parameters.¹⁹ Energy and temperature units are chosen such that Boltzmann's constant $k_B = 1$.

B. Algorithm

To investigate the kinetics of the phase transformation, we perform kinetic Monte Carlo simulations,³² where the transition probability for an elementary step is given by the Glauber acceptance probability³³

$$P = \frac{1}{1 + \exp[(E_f - E_i)/k_B T]}, \quad (5)$$

with E_f and E_i the configurational energies in the final and the initial configurations, respectively. We choose this dynamic for the sake of consistency with earlier work.¹⁵ Other dynamics that are commonly used in studies of electrochemical adsorption, such as the one-step dynamic^{34,35} and the transition dynamic algorithm^{36,37} also contain a *local* transition barrier and are commonly known as Arrhenius dynamics. For further discussion and applications of such dynamics, see, e.g., Refs. 1,6,38,39.

Two kinds of elementary steps are considered: an adsorption/desorption step, which corresponds to a non-conserved order parameter, and a diffusion step to a nearest-neighbor position, which conserves the order parameter.⁴⁰ A new configuration is chosen by randomly picking a lattice site and proposing a trial step: either, with probability $1/(R+1)$, an adsorption/desorption step or, with probability $R/(R+1)$, a diffusion step to a randomly chosen nearest-neighbor position. Thus, the ratio of the diffusion attempt probability to the adsorption/desorption attempt probability equals R . Explicitly, we propose adsorption when we choose an empty site for an adsorption/desorption step, and desorption when we choose an occupied site – there is no second-layer growth. When we choose an empty site for a diffusion step, the initial configuration is maintained – vacancies do not diffuse. Only after attempting an adsorption/desorption step is the simulation clock updated by one Monte Carlo step (mcs); hence, a higher diffusion rate R does not slow down the time scale for adsorption/desorption, which is the physically relevant time scale for the phase transformation. After L^2 mcs, the simulation time thus has increased by one *Monte Carlo step per site* (MCSS). Hence, one MCSS means in our simulations one adsorption/desorption attempt per site.

We start our simulations with an empty lattice, set the electrochemical potential to $\mu = \mu_0 + 0.4$, and let the system relax toward the stable configuration. We sample the time development of the coverage θ (the appropriate order parameter of the system, equivalent to φ in KJMA theory) and, at certain coverages, evaluate the cluster-size distribution, using the Hoshen-Kopelman algorithm.⁴¹ We perform model calculations for various values of R from 0 to 1000. Every calculation is the average over 100 independent simulation runs.

One of our goals is the understanding of the electrochemical deposition and subsequent dissolution of metal ad-sorbates after short pulses of the electrode potential. To that end, in addition to the constant-potential simulations

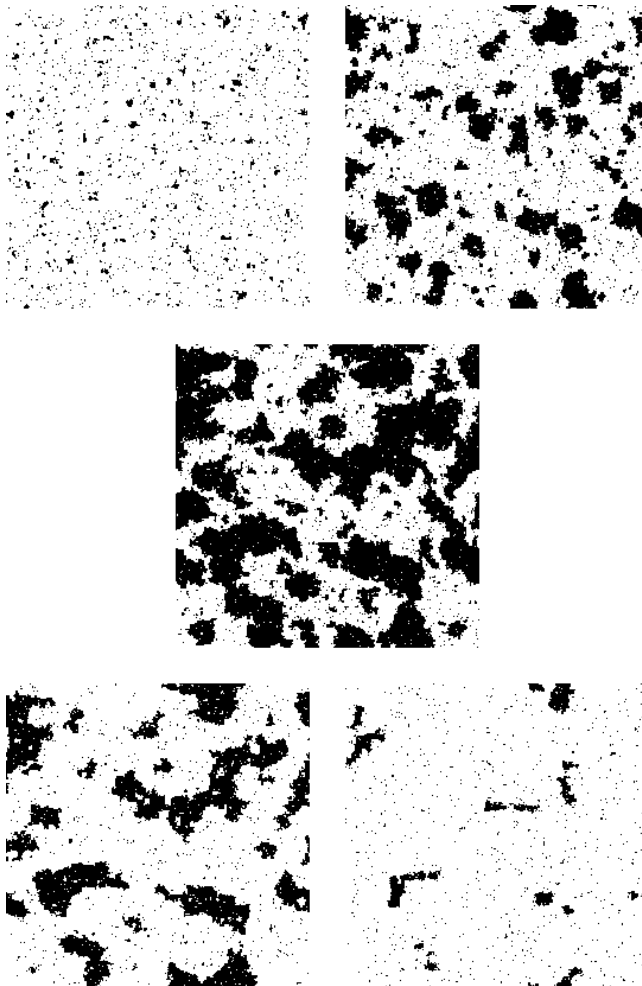


FIG. 1: Snapshots at different stages of the phase transformation during the potential-pulse simulations. $R = 0$. Coverages (from upper left to lower right): $\theta = 0.05$, $\theta = 0.25$ and $\theta = 0.5$ during the adsorption step, $\theta = 0.25$ and $\theta = 0.05$ during the desorption step.

described in the previous paragraph, we perform potential-pulse simulations for values of R from 0 to 10 000 starting from a metastable low-coverage configuration (result of an equilibration at $\mu = \mu_0 - 0.4$), set $\mu = \mu_0 + 0.4$ and wait until a certain coverage θ_s is reached. Then, we switch back to $\mu = \mu_0 - 0.4$, at which the adsorbate desorbs again, and let the system equilibrate.

III. RESULTS

In this section, we present the results of our model simulations for the constant-potential and the potential-pulse cases. Snapshots of the adsorbate morphology at different time steps (Fig. 1) show the nucleation, growth, and coalescence of clusters of quite irregular shapes (a more detailed discussion of this figure follows in Sec. III B 1). It has been established, however, that the classical KJMA theory gives a good statistical description of phase transformation with microscopic dynamics, at least at its earlier stages and in the absence of diffusion, even though it assumes the growth of circular droplets.¹⁵ Despite that the KJMA theory does not make assumptions about the nucleation and growth mechanisms, it is not clear how far it will hold when adsorbate diffusion is included in the kinetics of the lattice-gas model. We shall address this question in the following.

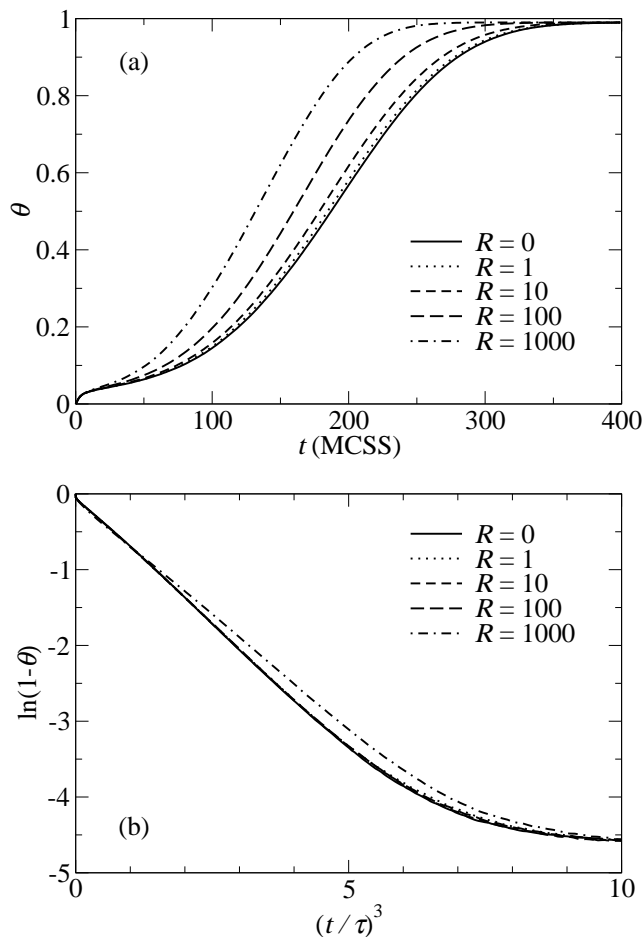


FIG. 2: Time development of the coverage during constant-potential simulations. (a) Linear plot vs time. (b) Logarithmic plot of fraction of uncovered area vs cube of normalized time.

TABLE I: Metastable lifetime for different diffusion rates R : τ_θ from $\theta = 0.5$ in constant-potential simulations and τ_p from peak position in potential-pulse simulations.

R	τ_θ (MCSS)	τ_p (MCSS)
0	187	184
1	185	184
10	179	177
100	160	160
1000	132	130
10 000		111

A. Phase-transformation kinetics

Monte Carlo results for the time development of the coverage at constant potential [Fig. 2(a)] apparently show the shape familiar from KJMA theory,¹⁰ but with an acceleration of the phase transformation due to diffusion. For a diffusion rate of $R = 10$ the effect is not very marked, but it becomes quite pronounced for higher R . In order to quantify the effect, we define the metastable lifetime τ as the time when the coverage reaches $\theta = 1/2$. The results are shown in Table I. The lifetime τ decreases weakly from $R = 0$ to $R = 10$, and then more strongly for larger R .

KJMA theory predicts a linear dependence of the logarithm of the area fraction of the untransformed phase $\ln(1-\theta)$ on t^n with the Avrami exponent $n = 3$ [Eqs. (1) and (2)]. In order to distinguish a change in the linear dependence from the acceleration of the phase transformation, we normalize the time scales to the metastable lifetime τ . Figure 2(b)

TABLE II: Kinetic parameters of the KJMA theory from fits of the phase transformation plots similar to Fig. 2(b) for different diffusion rates R . I nucleation rate, v linear growth rate, τ metastable life time.

R	Iv^2 (MCSS ³)	$Iv^2\tau^3$
0	9.1×10^{-8}	0.59
1	9.5×10^{-8}	0.59
10	1.0×10^{-7}	0.59
100	1.5×10^{-7}	0.59
1000	2.5×10^{-7}	0.56

shows almost perfect data collapse up to $R = 100$. At larger R , the slope is initially steeper. This corresponds to a relatively higher increase of the transformation rate, which levels off at $t \approx \tau$. To obtain quantitative information on the kinetics, we perform for all values of R unweighted least-squares fits to straight lines of the corresponding data points with the time scale unnormalized. The slopes give the product Iv^2 . From Eqs. (1) and (2), the contributions of the nucleation and growth rates, I and v , to the acceleration of the phase transformation cannot be distinguished. For a separate estimate of I and v , one needs to know the variance of the order parameter,¹⁵ which we did not sample in our simulations.

The fits have to be restricted to a certain time interval. Around $t = \tau$, the plots show a slight kink, a result of surface tension effects around the percolation coverage, which disturb the independent growth of the droplets. Therefore, we choose $0.9 \times \tau$ as the upper limit. At very short times the system relaxes quickly to the metastable state. Therefore, we choose the lower time limit by stepwise decreasing it until χ^2 per degree of freedom starts to increase steeply. We here refrain from correcting for the background of the metastable phase, in contrast to Ref. 15.

The results for Iv^2 shown in Table II reflect the acceleration of the phase transformation. The product Iv^2 is inversely proportional to the cube of the metastable lifetime τ , and as long as the dynamics of the phase transformation do not change qualitatively, the situation is tantamount to a mere rescaling of the time scale. Then, the film morphology at the same coverage should not depend on R . The product $Iv^2\tau^3$ is constant for $R \leq 100$, but differs at $R = 1000$, indicating a qualitative change in the phase-transformation dynamics for large R . Accordingly, we find that the curve for the same R fits less well to a straight line, so that the fitting interval is much shorter. We will return to this point in the next paragraph. In Sec. III B 2 we will show that this change coincides with a change of the film morphology.

The adsorption step of the potential-pulse calculations is equivalent to the constant-potential simulations. After the potential switch, the adsorbate desorbs, resulting in peak-shaped coverage curves, as we demonstrate for a switching coverage of 0.5 in Fig. 3(a). The peak position gives another estimate for the metastable lifetime τ (Table I). It coincides with the former estimate. In the absence of diffusion, the desorption is faster than the adsorption – the desorption can proceed without previous nucleation by simple shrinking of the clusters. The asymmetry in the kinetics between adsorption and desorption decreases with increasing R and is very small at $R = 10\,000$ [Fig. 3(b)]. At this diffusion rate, the decay of the metastable phase seems to be much better described by an Avrami exponent $n = 2$, consistent with instantaneous nucleation (Fig. 4).

During the growth of the adsorbate phase, nucleation may be effectively inhibited in the *capture zones* around clusters, and the size of these zones depends on the diffusion rate.^{42,43} Concerning the apparent Avrami exponent $n = 2$ for $R = 10\,000$, one may speculate that nucleation is initially very fast, but gets inhibited quickly on the whole surface, which is completely covered by the capture zones of existing clusters. The result is instantaneous, though homogeneous nucleation. The subsequent adsorption kinetics are governed solely by the growth rate, as is the case for the desorption kinetics after the potential step. This explains the almost symmetric coverage curves for $R = 10\,000$ [Fig. 3(b)].

B. Cluster-size distributions

We characterize the film morphology by means of the cluster-size distributions. We show the number densities, i.e. the total number of clusters of size s on the finite lattice, divided by the number of lattice sites. This equals the probability of finding on a site the center of a cluster of size s . The size s is the number of particles in the cluster. Due to the low number densities for large cluster sizes, we use a growing bin size for the histograms, resulting in an equal distribution of data points on a logarithmic scale. We show results for the potential-pulse simulations.

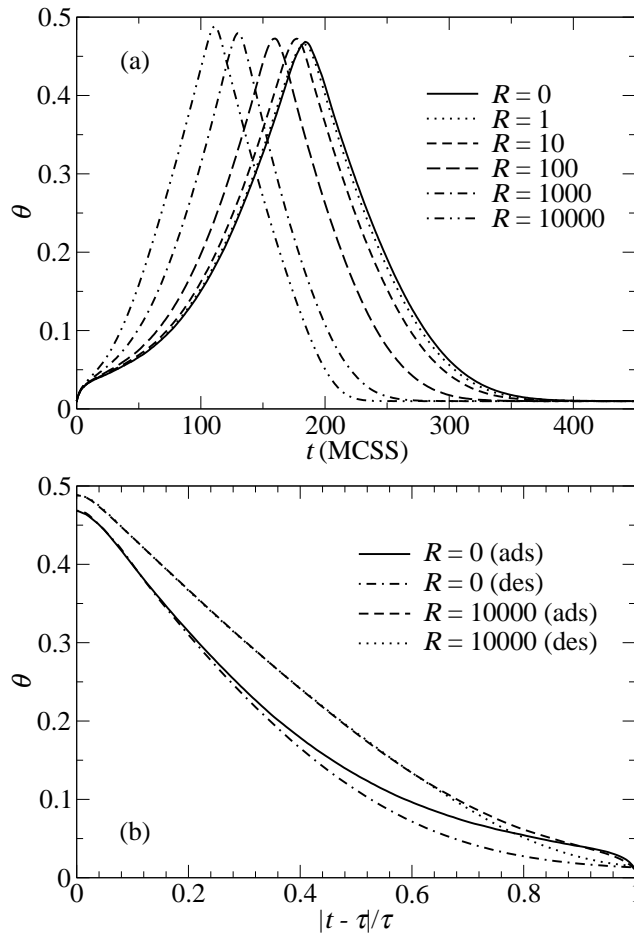


FIG. 3: Time development of the coverage during potential-pulse simulations with switching coverage $\theta_s = 0.5$. (a) Linear. (b) Mirrored at τ and normalized with τ . Curves labeled (ads) during adsorption step, curves labeled (des) during desorption step.

1. In the absence of diffusion

In the absence of diffusion, we show the evolution of the cluster-size distributions at different stages of the course of the potential-pulse simulations as log-log plots in Fig. 5. During the adsorption step, the maximum cluster size increases with time, as existing clusters grow to larger sizes. The number densities of the cluster sizes that had been present previously decrease. This indicates that with time fewer clusters nucleate and grow into a certain size interval than grow out of it. In the early stages of the desorption step, it can be clearly seen that, while the densities of the largest and of medium-sized and small clusters are decreasing, some intermediately large clusters (around $s = 1000$) still gain in population. This is also true in the presence of diffusion (not shown). Later, the distribution gets consumed from the large-cluster side. Hence, the distributions at equal coverage differ markedly between the adsorption and the desorption step. This difference is clearly reflected in the snapshots of the film morphology in Fig. 1, when comparing equal coverages during adsorption and desorption. The latter show fewer, but larger clusters. These snapshots also demonstrate the effect of coalescence during adsorption on the morphology – individual structures that form larger aggregates at later times can be clearly identified. Conversely, during desorption, dissociation of smaller clusters from larger aggregates may occur. A complete theory of cluster-size distributions, which we do not aim to present here, must consider these complications. We conclude that, during adsorption, existing clusters grow to larger sizes and may undergo coalescence, while new and thus smaller clusters can only appear on the untransformed area, thus with reduced probability. In the early stages of desorption, ripening of the morphology occurs in parallel with a decrease of the coverage, while later, clusters of all sizes shrink at constant rates.

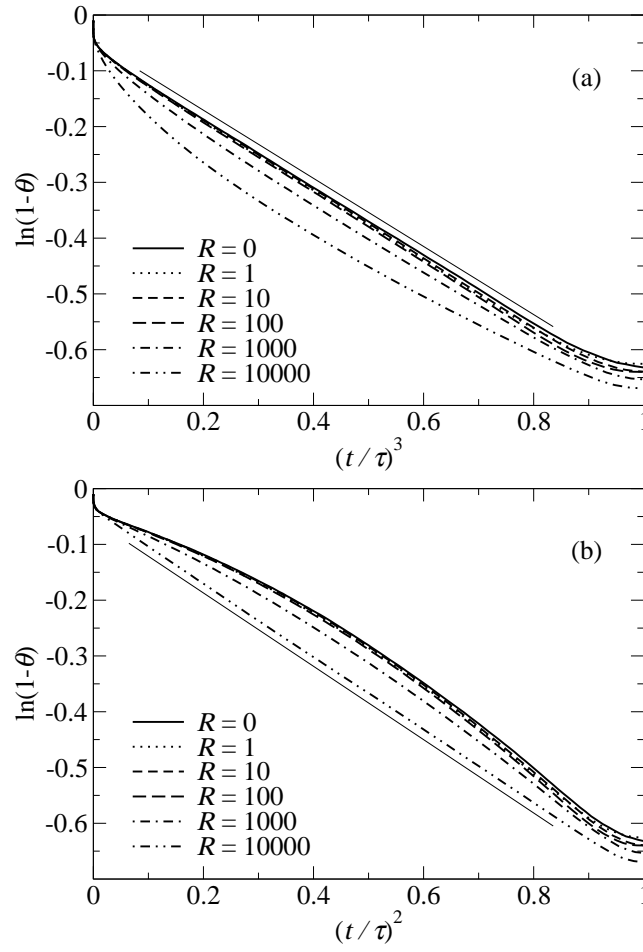


FIG. 4: Time development of the coverage during potential-pulse simulations up to τ . Logarithmic plot of fraction of uncovered area vs (a) cube (b) square of normalized time. The thin straight lines are guides to the eye.

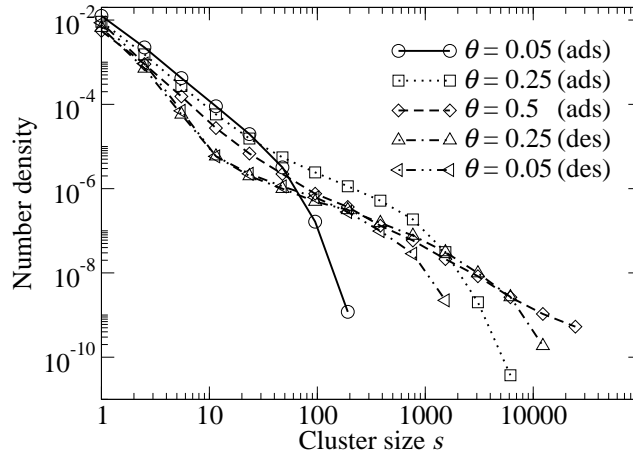


FIG. 5: Cluster-size distributions (number of clusters of size s per unit area) for potential-pulse simulation during the adsorption step (ads) and the desorption step (des). Switching coverage $\theta_s = 0.5$, diffusion rate $R = 0$.

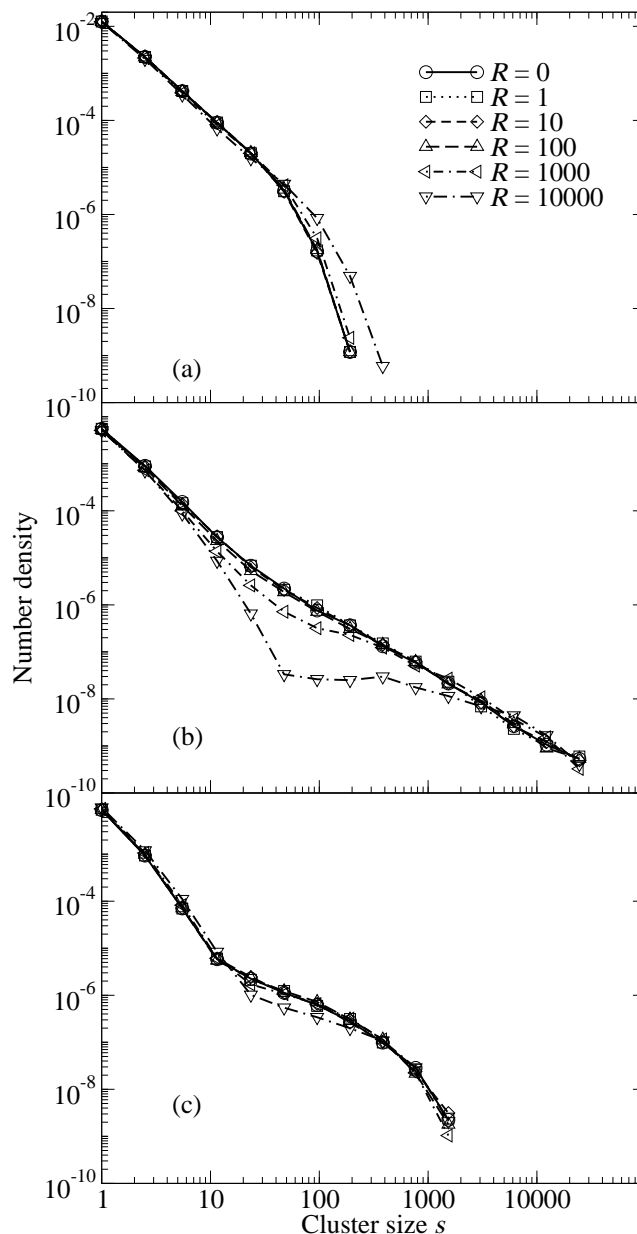


FIG. 6: Cluster-size distributions (number of clusters of size s per unit area) for potential-pulse simulations with switching coverage $\theta_s = 0.5$. (a) $\theta = 0.05$ (during adsorption step). (b) $\theta = 0.5$ (potential switch). (c) $\theta = 0.05$ (during desorption step).

2. In the presence of diffusion

For the potential-pulse simulations in the presence of diffusion, results for different diffusion rates at $\theta = 0.05$ during adsorption, $\theta = 0.5$ (the switching coverage), and $\theta = 0.05$ during desorption are shown in Fig. 6 as log-log plots. In the early stages of growth, we find that for fast diffusion rates ($R \geq 1000$), the maximum cluster sizes present are larger [Fig. 6(a)]. At later stages, there is a marked reduction through fast diffusion of the densities of medium-sized clusters, together with an increase of the densities of large clusters [Fig. 6(b)]. In accordance with this observation, snapshots of the phase transformation show a coarser morphology for $R = 1000$ than for $R = 0$ (Fig. 7). Near the end of the reverse step, the reduction of the amount of medium-sized clusters prevails, but much weaker, such that the morphologies for different R get more similar during desorption [Fig. 6(c)]. For $R \leq 100$, the distributions are virtually indistinguishable from the case without diffusion. This indicates that the phase-transformation dynamics are similar and just proceed on a faster time scale (Sec. III A).

We find the reduction of medium-sized clusters more likely to be a result of increased coalescence rates than of a

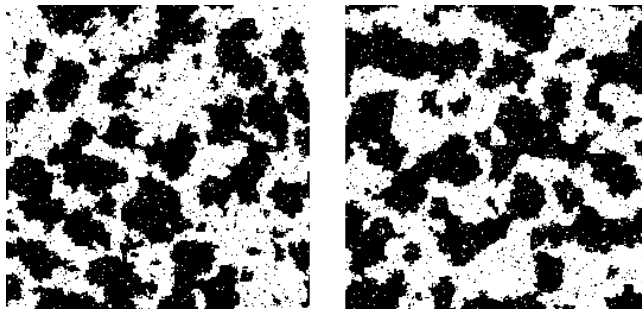


FIG. 7: Snapshots for diffusion rates $R = 0$ (left) and $R = 1000$ (right). In both cases, $\theta = 0.5$.

TABLE III: Reduction of the monomer number density n_1 relative to the untransformed surface fraction. R diffusion rate, θ coverage. See Sec. III C 1.

R	θ	$n_1(\theta)$	$\frac{1-\theta}{1-0.05}$	$\frac{n_1(\theta)}{n_1(0.05)}$
0	0.05	1.25×10^{-2}	1	1
	0.25	9.10×10^{-3}	0.79	0.72
	0.5	5.53×10^{-3}	0.53	0.44
1000	0.05	1.24×10^{-2}	1	1
	0.25	8.60×10^{-3}	0.79	0.69
	0.5	5.51×10^{-3}	0.53	0.41

change of the radius-dependent growth law of the clusters. While the former can be a result of a collective motion of clusters established by edge diffusion or of dissociation and diffusion of monomers and is well established in surface science,^{44,45,46} the latter would imply an unphysical slowing-down of growth only at medium sizes.

We have seen that diffusion affects the cluster-size distributions only at diffusion rates high enough that also the phase-transformation kinetics cross over from continuous to initial nucleation, $R \geq 1000$ (Sec. III A). Lower diffusion rates speed up the dynamics without changing them qualitatively. A rough estimation considering the number densities of monomers suggests that at these lower rates, diffusion is still not more frequent than adsorption/desorption, as the mere numerical values of R naïvely might suggest.

C. Subcritical cluster distributions

Unlike the supercritical droplets, whose size distribution is governed by the phase-transformation dynamics, the subcritical droplets can be considered to be quasi-equilibrium fluctuations. This allows a thermodynamic approach for a theoretical description of their size distribution. We first show simulation results of the size distributions. Second, we calculate their theoretical quasi-equilibrium distribution within a lattice-animal model.

1. Simulation results

We show the number densities, as explained in Sec. III B, of the subcritical clusters for potential-pulse simulations with a switching coverage of $\theta_s = 0.5$ in Fig. 8. At all stages of the simulation, the size distribution of small clusters decreases monotonically with increasing size. The distribution develops with time. During the adsorption step, the number densities decrease. This decrease is somewhat greater than expected from the decrease of the untransformed surface fraction. Column 4 in Table III shows the fraction to which the free surface gets reduced compared to $\theta = 0.05$, and column 5 shows the corresponding reduction of the monomer density. The reduction of the monomer density is always greater than the reduction of the free surface, and it is enhanced by increasing diffusion rate. This indicates that in a capture zone close to an existing cluster nucleation is suppressed, since aggregation to the cluster is more likely. The size of the capture zones is increased by diffusion. During the desorption step, the number densities of small clusters are generally further diminished (with the exception of monomers and dimers, whose densities increase). Again, in the course of desorption, the distributions with and without diffusion approach each other.

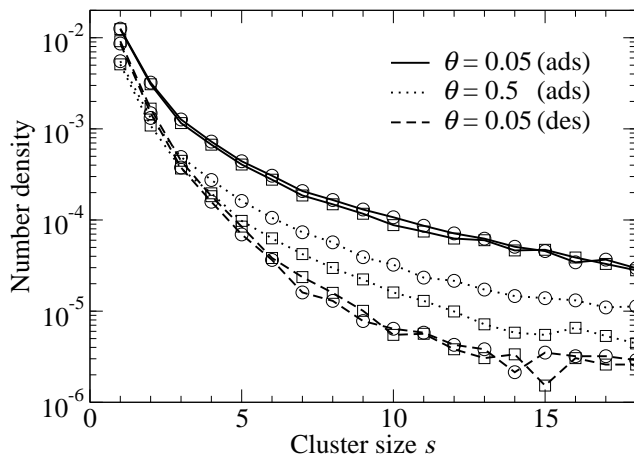


FIG. 8: Subcritical cluster-size distributions (number of clusters of size s per unit area) for $R = 0$ (circles) and $R = 1000$ (squares) at different stages of the potential-pulse simulations. Curves labeled (ads) during the adsorption step, curves labeled (des) during the desorption step.

2. Lattice-animal model

The cluster-size probability distribution gives the probability $P(s)$ that a subcritical cluster is of size s , and it is normalized such that the sum of all probabilities equals 1. To calculate it, we need an expression for the free energy $F(s)$ of a cluster of size s , since

$$P(s) \propto \exp(-F(s)/k_{\text{B}}T). \quad (6)$$

The theoretical prediction from droplet theory [Eq. (3)], in two dimensions, using $\sqrt{s/\pi}$ as an effective radius r and the exact zero-field Ising values for σ_0 and $\Delta\theta$, is shown in Fig. 9. The agreement is rather poor. Since the surface tension, which is a macroscopic quantity, may not be a good description for such small clusters, we seek a better statistical-mechanical expression for the cluster free energy. If we knew all possible configurations of a cluster of size s and their numbers of bonds to nearest-neighbor unoccupied sites (including holes) t , we could compute its restricted partition function exactly as

$$Z(s) = \exp\left(\frac{s(\mu - \mu_0)}{k_{\text{B}}T}\right) \sum_t w(s, t) \exp\left(-\frac{t\phi}{2k_{\text{B}}T}\right). \quad (7)$$

More specifically, we need to know the number $w(s, t)$ of degenerate clusters with same s and t . These numbers are very high unless s is very small. As a consequence, even with the help of computers, they are accessible only up to moderate values of s . Generating these configurations is known as counting lattice animals.^{25,47,48,49,50} In the lattice-animal literature (see, e.g., Ref. 51), the perimeter, if considered, is usually defined as the number of unoccupied nearest-neighbor sites and not as the number of bonds to these sites, and only $w(s)$ is known. For the calculation of $w(s, t)$, we use the algorithm of Redner.⁵² We show the results for animals up to $s = 21$ in Table IV. The computation took about 65 hours of CPU time on an Intel Xeon-based workstation. The $w(s)$ from our calculations are in accord with the known results.^{49,50} From the partition function, the free energy is calculated as

$$F(s) = -k_{\text{B}}T \ln Z(s), \quad (8)$$

so that

$$P(s) = Z(s) / \sum_{s=1}^{s^*} Z(s), \quad (9)$$

summing up to the critical cluster size s^* . This calculation, as the droplet theory, assumes non-interacting subcritical clusters which are in quasi-equilibrium throughout the course of the phase transformation, an assumption that should be better fulfilled at higher temperatures, as is the case in our simulations. The resulting cluster-size probability distribution is shown and compared to simulation results in Fig. 9. At early times and in the absence of diffusion,

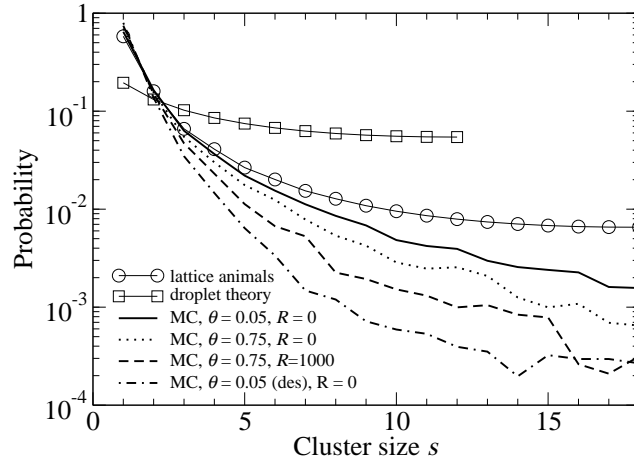


FIG. 9: Subcritical cluster-size probability distributions (probability that a subcritical cluster is of size s): Monte-Carlo results and theoretical predictions from droplet theory and from counting lattice animals. Curve labeled (des) during the desorption step, others during the adsorption step.

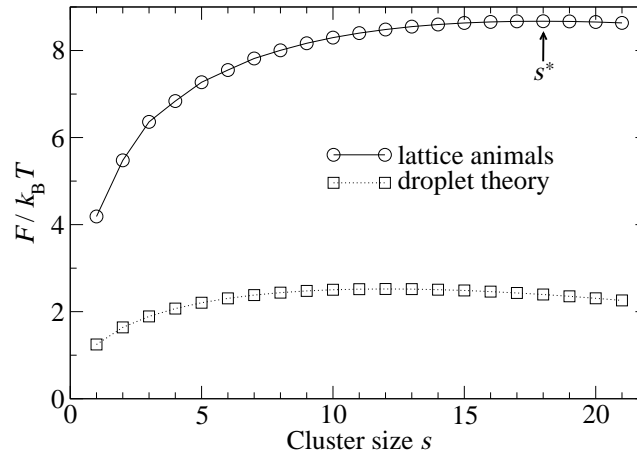


FIG. 10: Free energy of small clusters according to droplet theory and from counting lattice animals. The critical cluster size is labeled s^* .

the agreement is reasonable (note the logarithmic scale). The trends that we observed for the number densities are reflected as an increasing reduction of the probabilities with increasing cluster size for later times, in the presence of diffusion, and during desorption, respectively. We can attribute these trends to increasing deviations from the quasi-equilibrium distribution – the larger subcritical clusters are consumed faster than they are produced, or during desorption, the small clusters are produced faster than they disappear (remember their increase in absolute density). In contrast, the predictions of droplet theory are way off. This is a consequence of the surface-tension contribution to the free energy of the clusters (Fig. 10); surface fluctuations from the continuum description, which contribute to the partition function, are unphysical on the discrete lattice for small clusters. In the lattice-animal model, the maximum of the free energy is shifted to larger clusters compared to droplet theory, thus giving a critical cluster size of 18 instead of 12. In both cases, the free energy changes very little in the neighborhood of the critical cluster. An approach analogous to the one presented in this section was independently developed in Ref. 25 (with $w(s, t)$ computed up to $s = 17$).

IV. SUMMARY AND CONCLUSIONS

We have performed kinetic Monte Carlo simulations of a square lattice-gas model using Glauber dynamics to investigate the decay of a metastable low coverage phase. The model, which contains adsorption/desorption and nearest-neighbor diffusion moves, is used to qualitatively describe the electrosorption and subsequent dissolution of

TABLE IV: Number w of configurations of lattice animals of size s and perimeter t . For the definition of the perimeter, see Sec. III C 2.

s	t	$w(s, t)$	s	t	$w(s, t)$	s	t	$w(s, t)$	s	t	$w(s, t)$
1	4	1	12	16	151	16	24	303 068	19	32	161 217 996
2	6	2		18	2086		26	1 563 218		34	506 666 828
3	8	6		20	13 034		28	6 095 764		36	1 230 292 398
4	8	1		22	58 742		30	18 173 796		38	2 044 899 048
	10	18		24	163 494		32	36 285 432		40	1 946 892 842
5	10	8		26	268 352		34	42 120 340	20	18	2
	12	55	13	16	68	17	18	88		20	426
6	10	2		18	1392		20	3010		22	12 456
	12	40		20	11 789		22	36 112		24	152 400
	14	174		22	63 256		24	276 464		26	1 262 276
7	12	22		24	250 986		26	1 603 984		28	8 194 358
	14	168		26	633 748		28	7 477 928		30	44 227 470
	16	570		28	942 651		30	26 922 156		32	197 485 313
8	12	6	14	16	22		32	74 496 544		34	731 782 776
	14	134		18	864		34	139 297 108		36	2 166 643 248
	16	677		20	9354		36	150 682 450		38	4 965 061 010
	18	1908		22	62 396	18	18	30		40	7 822 910 077
9	12	1		24	297 262		20	1728		42	7 027 047 848
	14	72		26	1 056 608		22	26 906	21	20	187
	16	656		28	2 448 760		24	236 256		22	7648
	18	2708		30	3 329 608		26	1 559 888		24	115 504
	20	6473	15	16	6		28	8 193 956		26	1 068 896
10	14	30		18	456		30	35 016 382		28	7 664 819
	16	482		20	7036		32	117 417 380		30	45 205 960
	18	3008		22	54 908		34	303 516 966		32	225 345 274
	20	10 724		24	317 722		36	534 018 776		34	941 355 540
	22	22 202		26	1 359 512		38	540 832 274		36	3 281 439 844
11	14	8		28	4 401 192	19	18	8		38	9 193 698 004
	16	310		30	9 436 252		20	914		40	19 960 812 568
	18	2596		32	11 817 582		22	18 756		42	29 902 719 200
	20	13 456	16	16	1		24	194 614		44	25 424 079 339
	22	42 012		18	218		26	1 427 768			
	24	76 886		20	4748		28	8 446 952			
12	14	2		22	46 352		30	40 680 552			

metal ions onto a metal substrate in potential-pulse experiments. We have observed the phase-transformation kinetics and the size distributions of sub- and supercritical clusters. The results have been compared to the KJMA theory.

Nearest-neighbor diffusion speeds up the phase transformation. At low and moderate diffusion rates, the kinetics are well described by the KJMA theory for continuous nucleation. At high diffusion rates, we find a crossover to kinetics that resemble initial nucleation. In the former case, the cluster-size distributions are virtually indistinguishable from each other, but in the latter case, the densities of medium-sized clusters get reduced in favor of large clusters. At the same coverage, the morphology is coarser during the desorption step than during the adsorption step. The crossover to initial nucleation is likely to be a consequence of the diffusion-rate dependence of the size of the capture zones of clusters. When the diffusion rate increases, the capture zones get larger, and for very fast diffusion rates, they might become space-filling already in early stages of the phase transformation.

We have calculated the free energies of subcritical clusters from their exact restricted partition functions, which we obtain from counting lattice animals. This enables us to calculate a theoretical prediction of the subcritical cluster-size probability distribution. The prediction is in reasonable agreement with simulation results, apart from some well understandable deviations from the quasi-equilibrium distributions. In contrast, classical droplet theory fails, since the macroscopic surface tension is a poor description for the discrete microscopic clusters.

Berthier et al.²⁴ use a similar way as we for the calculation of subcritical cluster distributions. To obtain the number density of clusters of size s , they consider the configurational entropy of the ground and the first two excited states. These are the clusters with the three lowest perimeters t . Compared to our partition function, which considers all possible configurations (up to the highest excited state), their summation is incomplete for $s > 7$. Moreover, many of their weights for the excited states are too low. Since they do not specify the method of counting the

accessible configurations, the origin of the discrepancy is unclear, but it seems that they miss some configurations. As a consequence, the free energies obtained by their method are erroneously non-monotonic and too high.

The experimentally observed post-deposition dynamics after a potential pulse,¹⁷ which result in the continued growth of large clusters while small clusters already tend to dissolve, are clearly reproduced by our simulations. Though it is not necessary to explicitly include surface diffusion under control of the electrochemical potential to establish lateral mass transport, we find diffusion more likely to be the dominant mechanism under the experimental conditions. However, in our simulations, coverages are much higher than in the experiment. While time scales of adsorption and desorption in the experiment are rather different, in our model they are necessarily much more similar, since adsorption and desorption proceed with very similar mechanisms.

Our model calculations are a first step toward including diffusion into the microscopic dynamics of a kinetic lattice-gas (or Ising) model and to investigate its influence on the applicability of the KJMA theory. Still, calculations over a larger range of fields and a more stringent analysis are required.¹⁵ To support our hypotheses about the interplay between diffusion, nucleation, and spatial correlation, more microscopic information, like on nucleation events and the fate of individual clusters, should be obtained from the simulations. For a more meaningful description of experiments, a closer reproduction of experimental conditions is desirable.

Acknowledgments

This work was supported in part by National Science Foundation Grant No. DMR-0240078, and by Florida State University through its Center for Materials Research and Technology and School of Computational Science.

-
- ¹ G. Brown, P. A. Rikvold, S. J. Mitchell, and M. A. Novotny, in *Interfacial Electrochemistry: Theory, Experiment, and Applications*, edited by A. Wieckowski (Marcel Dekker, New York, 1999), pp. 47–61.
- ² P. A. Rikvold, G. Brown, and S. J. Mitchell, in *Encyclopedia of Surface and Colloid Science*, edited by A. Hubbard (Marcel Dekker, New York, 2002), pp. 4814–4824.
- ³ C. Ratsch and J. A. Venables, *J. Vac. Sci. Technol. A* **21**, S96 (2003).
- ⁴ S. Wang and P. A. Rikvold, *Phys. Rev. B* **65**, 155406 (2002).
- ⁵ S. Wang, Y. Cao, and P. A. Rikvold, *Phys. Rev. B* (in press).
- ⁶ S. J. Mitchell, G. Brown, and P. A. Rikvold, *Surf. Sci.* **471**, 125 (2001).
- ⁷ I. Abou Hamad, Th. Wandlowski, G. Brown, and P. A. Rikvold, *J. Electroanal. Chem.* **554-555**, 211 (2003).
- ⁸ M. T. M. Koper, *J. Electroanal. Chem.* **450**, 189 (1998).
- ⁹ A. N. Kolmogorov, *Bull. Acad. Sci. USSR, Phys. Ser.* **1**, 335 (1937).
- ¹⁰ W. A. Johnson and R. F. Mehl, *Trans. Am. Inst. Min. Metall. Eng.* **135**, 416 (1939).
- ¹¹ M. Avrami, *J. Chem. Phys.* **7**, 1103 (1939).
- ¹² M. Avrami, *J. Chem. Phys.* **8**, 212 (1940).
- ¹³ M. Avrami, *J. Chem. Phys.* **9**, 177 (1941).
- ¹⁴ P. A. Rikvold, H. Tomita, S. Miyashita, and S. W. Sides, *Phys. Rev. E* **49**, 5080 (1994).
- ¹⁵ R. A. Ramos, P. A. Rikvold, and M. A. Novotny, *Phys. Rev. B* **59**, 9053 (1999).
- ¹⁶ V. A. Shneidman, K. A. Jackson, and K. M. Beatty, *Phys. Rev. B* **59**, 3579 (1999).
- ¹⁷ Y. He and E. Borguet, *J. Phys. Chem. B* **105**, 3981 (2001).
- ¹⁸ P. A. Rikvold and B. M. Gorman, in *Annual Reviews of Computational Physics*, edited by D. Stauffer (World Scientific, Singapore, 1994), Vol. 1, pp. 149–191.
- ¹⁹ L. Onsager, *Phys. Rev.* **65**, 117 (1944).
- ²⁰ C. N. Yang, *Phys. Rev. B* **85**, 808 (1952).
- ²¹ S. Wonzak, R. Strey, and D. Stauffer, *J. Chem. Phys.* **113**, 1976 (2000).
- ²² V. A. Shneidman, K. A. Jackson, and K. M. Beatty, *J. Chem. Phys.* **111**, 6932 (1999).
- ²³ V. A. Shneidman and R. K. P. Zia, *Phys. Rev. B* **63**, 085410 (2001).
- ²⁴ F. Berthier, B. Legrand, J. Creuze, and R. Tétot, *J. Electroanal. Chem.* **561**, 37 (2004).
- ²⁵ V. A. Shneidman and G. M. Nita, *J. Chem. Phys.* **121** (21), (2004), in press.
- ²⁶ M. C. Bartelt and J. W. Evans, *Phys. Rev. B* **54**, R17359 (1996).
- ²⁷ E. Pineda, T. Pradell, and D. Crespo, *Philos. Mag. A* **82**, 107 (2002).
- ²⁸ M. Fanfoni and M. Tomellini, *Eur. Phys. J. B* **34**, 331 (2003).
- ²⁹ T. D. Lee and C. N. Yang, *Phys. Rev.* **87**, 410 (1952).
- ³⁰ For a spin $s_i = \pm 1$ Ising model with z nearest neighbors (here, $z = 4$) and \mathcal{N} sites, coupling constant J and external magnetic field H , the mapping between the models is $\mathcal{H}_I = \mathcal{H}_{LG} + \frac{1}{2}\mathcal{N}(\mu - \frac{1}{2}\mu_0)$, $c_i = \frac{1}{2}(s_i + 1)$, $\phi = 4J$, $\mu - \mu_0 = 2H$, and $\mu_0 = -2zJ$.
- ³¹ Corresponding, in magnetic language, to $J = 1$ and $|H| = 0.2$.¹⁸
- ³² K. Binder and D. W. Heermann, *Monte Carlo Simulations in Statistical Physics. An Introduction*, 3rd ed. (Springer, Berlin, 1997).
- ³³ R. J. Glauber, *J. Math. Phys.* **4**, 294 (1963).
- ³⁴ H. C. Kang and W. H. Weinberg, *J. Chem. Phys.* **90**, 2824 (1989).
- ³⁵ K. A. Fichtorn and W. H. Weinberg, *J. Chem. Phys.* **95**, 1090 (1991).
- ³⁶ T. Ala-Nissila, J. Kjoll, and S. C. Ying, *Phys. Rev. B* **46**, 846 (1992).
- ³⁷ T. Ala-Nissila and S. C. Ying, *Prog. Surf. Sci.* **39**, 227 (1992).
- ³⁸ I. Abou Hamad, G. Brown, and P. A. Rikvold, *Surf. Sci. Lett.* **572**, L335 (2004).
- ³⁹ G. M. Buendía, P. A. Rikvold, K. Park, and M. A. Novotny, *J. Chem. Phys.* **121**, 4193 (2004).
- ⁴⁰ J. D. Gunton, M. San Miguel, and P. S. Sahni, in *Phase Transitions and Critical Phenomena*, edited by C. Domb and J. L. Lebowitz (Academic Press, New York, 1983), Vol. 8.
- ⁴¹ J. Hoshen and R. Kopelman, *Phys. Rev. B* **14**, 3438 (1976).
- ⁴² J. W. Evans and M. C. Bartelt, *Phys. Rev. B* **66**, 235410 (2002).
- ⁴³ F. Family, M. A. Popescu, and J. G. Amar, *Physica A* **306**, 129 (2002).
- ⁴⁴ J.-M. Wen, S.-L. Chang, J. W. Burnett, J. W. Evans, and P. A. Thiel, *Phys. Rev. Lett.* **73**, 2591 (1994).
- ⁴⁵ W. W. Pai, A. K. Swan, Z. Zhang, and J. W. Wendelken, *Phys. Rev. Lett.* **79**, 3210 (1997).
- ⁴⁶ S. V. Khare and T. L. Einstein, *Phys. Rev. B* **54**, 11752 (1996).
- ⁴⁷ S. W. Golomb, *Polyominoes* (Scribner, New York, 1965).
- ⁴⁸ D. Stauffer, *Phys. Rep.* **54**, 1 (1979).
- ⁴⁹ D. H. Redelmeier, *Discrete Math.* **36**, 191 (1981).
- ⁵⁰ I. Jensen, *J. Stat. Phys.* **102**, 865 (2001).
- ⁵¹ M. F. Sykes and M. Glen, *J. Phys. A: Math. Gen.* **9**, 87 (1976).
- ⁵² S. Redner, *J. Stat. Phys.* **29**, 309 (1982).